KSME

Springer

Journal of Mechanical Science and Technology 37 (7) 2023

Original Article
DOI 10.1007/s12206-023-2207-6

Keywords:
· High-pressure aerostatic thrust bearing
· Boundary layer
· Thermal deformation
· Uneven temperature field
· Conjugate heat transfer
· Thermal conductivity

Correspondence to:
Liangbin Guo
guoliangbin@wust.edu.cn

Citation:
Guo, L., Chen, S. (2023). Study on thermal deformation of high-pressure aerostatic thrust bearing in uneven temperature field. Journal of Mechanical Science and Technology 37 (7) (2023) 3281~3293. http://doi.org/10.1007/s12206-023-2207-6

Received January 2nd, 2023
Revised February 26th, 2023
Accepted February 26th, 2023

† This paper was presented at International Session in KSME Annual Meeting 2022, ICC JEJU, Jeju, Korea & Online, November 9-12, 2022.
Recommended by Guest Editor Do-Nyun Kim

Study on thermal deformation of high-pressure aerostatic thrust bearing in uneven temperature field

Liangbin Guo[1,2] and Shanxiu Chen[3]

[1]Key Laboratory of Metallurgical Equipment and Control Technology, Ministry of Education, Wuhan University of Science and Technology, Wuhan 430081, China, [2]Hubei Key Laboratory of Mechanical Transmission and Manufacturing Engineering, Wuhan University of Science and Technology, Wuhan 430081, China, [3]School of Marxism, Wuhan University of Science and Technology, Wuhan 430065, China

Abstract As for high-pressure aerostatic thrust bearing, the notable increase of air supply pressure makes gas film pressure and flow velocity increase rapidly. The two assumptions of fully developed laminar boundary layer and isothermal flow in parallel gas film are no longer valid, which are generally considered suitable for aerostatic thrust bearing with low air supply pressure. Based on the coupling analysis of the air flow field in the channel clearance of the bearing and the conjugate heat transfer of the bearing discs, the development process and flow regime of the velocity boundary layer and the temperature boundary layer in the parallel gas film are investigated. The results of conjugate heat transfer analysis for bearing discs made of various materials show that, isotropic thermal conductivity is the main factor affecting the heat flux, temperature distribution on the interface between solid wall and high-speed airflow in the channel clearance, and the temperature gradient inside the bearing discs. Further research on the relationship between the net thermal deformation, net elastic deformation caused by gas film pressure as well as total deformations of the bearing discs and the material properties shows that, the coefficient of thermal expansion is a crucial parameter affecting the net thermal deformation, but the total deformations of bearing discs also depend on the pressure load exerted by gas film. In the range of the working conditions specified in this study, structural steel is a more suitable choice than stainless steel or invar. Consequently, this research provides meaningful guidance for the designs of high-pressure aerostatic thrust bearings.

1. Introduction

With the development of application of aerostatic thrust bearing towards high temperature, high speed and high air supply pressure, the generation and transmission of heat in the gas film has become increasingly significant, which leads not only to thermal deformation of the disc itself but also to changes in the bearing clearance and therefore in the characteristics of bearing [1-8]. Consequently, the working stability of aerostatic thrust bearing after applying thermal load and pressure load has gradually formed a crucial factor restricting its performance.

As for high-pressure aerostatic thrust bearing, the notable increase of air supply pressure makes gas film pressure and flow velocity increase rapidly, thus the speed of air in flow channel clearance develops from low subsonic to high subsonic or even supersonic. The two assumptions of fully developed laminar boundary layer and isothermal flow in parallel gas film are no longer valid, which are generally considered suitable for aerostatic thrust bearing with low air supply pressure. At the same time, there is an obvious temperature difference among various internal regions of the gas film, as well as between the gas film and the solid wall of the bearing discs. On the one hand, the uneven temperature field inside discs produces thermal deformation of the bearing discs, which also includes the deformation caused by the gas film pressure. On the other hand, the heat conduction inside the bearing discs and the convection heat transfer of the high-speed airflow are closely coupled through the fluid-solid interface, which is de-

fined as conjugate heat transfer (CHT) [9]. Thus, the analysis of thermal deformation of high-pressure aerostatic thrust bearing should be simplified to the combination of a steady state CHT problem and a static thermal deformation problem.

The term 'conjugate heat transfer (CHT)' refers to a heat transfer process involving an interaction of heat conduction within a solid body with any one of the free, forced, and mixed convection from its surface to a fluid flowing over it, which has attracted increasing attention [10-14]. In fact, the conjugate procedure is essential for any problem containing at least two interaction subjects because that is the only way to find the parameters on interface and the subsequent solution [12], which means the CHT is the basis for determining the uneven temperature field of the bearing discs.

Based on the coupling analysis of the air flow field in the channel clearance of the bearing and the conjugate heat transfer of the bearing discs, the development processes and flow regime of the velocity boundary layer and the temperature boundary layer in the parallel gas film are analyzed. As mechanical designers pay special attention to the influence of different material properties of bearing disc on the thermal deformation, in this study, the effect of isotropic thermal conductivity of disc material on characteristics of temperature field of bearing discs is carefully investigated. Furthermore, the influence of other material properties on thermal deformation is studied, and the reasonable material for the bearing is determined. This research gains a deeper understanding of the thermal deformation phenomenon of the high-pressure aerostatic thrust bearing and clarifies the inner mechanism of the effect of the material properties of bearing on the total deformation of discs, which consequently provides meaningful guidance for the design of the high-pressure aerostatic thrust bearing.

2. CHT analysis of the bearing

2.1 Configuration of high-pressure aerostatic thrust bearing

The schematic of high-pressure aerostatic thrust bearing is shown in Fig. 1. The bearing is composed of upper disc parts and lower disc parts, which are symmetrical with respect to the symmetric plane (14) of the gas film. Take the upper disc parts as an example, it is assembled by the upper anemostat (3), the upper gasket (5) and the upper disc (6) with a threaded connection. One end of the upper anemostat (3) is tightened upon the upper disc (6) by screw while the other end is connected with the external air supply pipe by tube joint so as to ensure the input of high-pressure air. The upper anemostat (3) closely resembles an axial convergent nozzle, and is used to rectify the airstream which comes from the external air supply pipe, so that the airstream can enter the upper air supply hole (4) at a nearly same speed. The contraction curve of the axisymmetric contraction section (2) of upper anemostat is designed according to Витощинский formula.

The contraction sections (7) and (13) not only form an axisymmetric structure about the symmetric axis, but also get a face-symmetric structure relative to the symmetrical plane (14) of gas film, which is why it is called double symmetric contraction section. This contraction sections (7) and (13) reduce the flow separation effectively during the steering process of the airstream, which make the axial low-speed airstream via supply hole to parallel gas film region smoothly accelerate to the radially high subsonic flow at the exit of the contraction sections (7) and (13). The contraction curves of the double symmetric contraction sections are designed according to the methodology proposed in the Ref. [6]. One end of the contraction section of upper disc (7) is tangent to the upper air supply hole (4), and the other end is tangent to the interface between the upper disc and parallel gas film (15), as shown in Fig. 1. The geometrical dimensions of the high-pressure aerostatic thrust bearing are listed in Table 1.

The 3D geometric model of the bearing is shown in Fig. 2. In order to successfully extract the calculation domain of internal

Table 1. Dimensions of the aerostatic thrust bearing.

Diameter of entrance of anemostat d_2 (mm)	20
Radius of air supply hole r_h (mm)	5
Radius of exit of contraction section r_t (mm)	29.798
Height of parallel gas film h_1 (mm)	0.2
Thickness of disc h_2 (mm)	30
Height of anemostat h_3 (mm)	70
Radius of bearing disc r_e (mm)	60

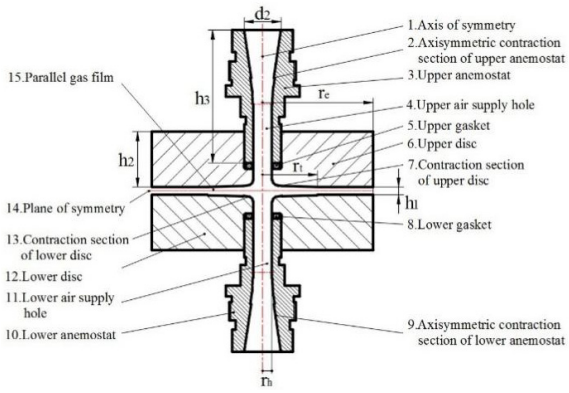

Fig. 1. Schematic of high-pressure aerostatic thrust bearing.

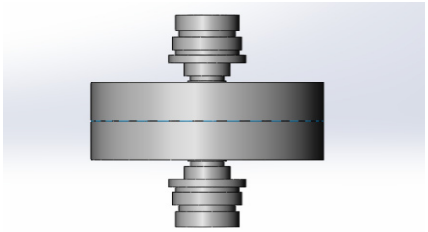

Fig. 2. 3D structural schematic of gas bearing.

Table 2. Names of surfaces in solid domain.

External surface of upper anemostat	Walloutsideanemostatup
External surface of lower anemostat	Walloutsideanemostatdown
Inlet end face of upper anemostat	Wallinletendup
Inlet end face of lower anemostat	Wallinletenddown
Symmetric plane of upper disc parts	Symmetrysolidup
Symmetric plane of lower disc parts	Symmetrysoliddown
External surface of upper disc	Walloutsidebearingup
External surface of lower disc	Walloutsidebearingdown
Interface between fluid and upper disc parts, at solid side	Interfacesolidup
Interface between fluid and lower disc parts, at solid side	Interfacesoliddown

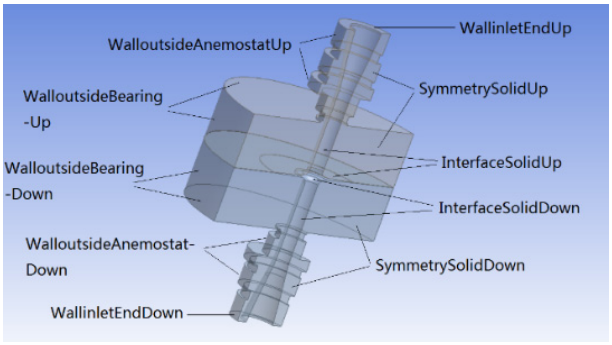

Fig. 3. Solution domain-one half of the whole 3D model.

flow field, a closed annular surface is established at the outlet of gas film.

For the double symmetric structure shown in Fig. 1, one half of the whole 3D model includes the fluid zone and the solid zone is selected as solution domain in order to facilitate the solving process, which is shown in Fig. 3.

It is important to name all kinds of boundaries of fluid domain and solid domain clearly, which is not easy due to confusion among diverse surfaces of solution domain model. According to Fig. 3, the names of surfaces in solid domain are listed in Table 2.

Fig. 4 shows fluid domain and names of diverse boundaries, the latter are listed in Table 3.

2.2 Mathematical model of CHT

2.2.1 Governing equations of fluid domain

In this study, the conservation form of the Favre-averaged Navier-Stokes equations for three-dimensional, steady, compressible flow is solved for the turbulent flow cases [15, 16]. The indicial notation form of these equations in the Cartesian coordinates is given by

$$\frac{\partial(\rho u_i)}{\partial x_i}=0 \tag{1}$$

Table 3. Names of surfaces in fluid domain.

Air inlet of upper anemostat	Upinlet
Air inlet of lower anemostat	Downinlet
Interface between fluid and upper disc parts, at fluid side	Interfacefluidup
Interface between fluid and lower disc parts, at fluid side	Interfacefluiddown
Air outlet of gas film	Outlet

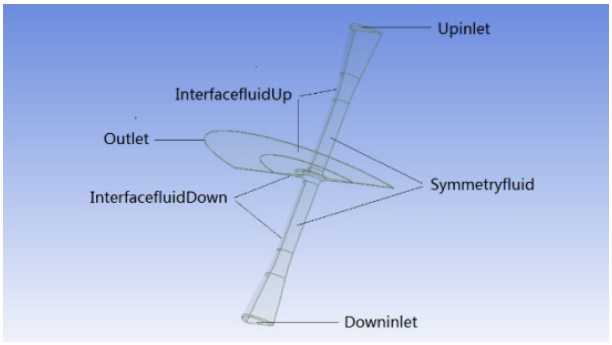

Fig. 4. Fluid domain of the solution domain model.

$$\frac{\partial\left(\rho u_i u_j\right)}{\partial x_j}=-\frac{\partial P}{\partial x_i}+\frac{\partial}{\partial x_j}\left[\mu\left(\frac{\partial u_i}{\partial x_j}+\frac{\partial u_j}{\partial x_i}-\frac{2}{3}\delta_{ij}\frac{\partial u_l}{\partial x_l}\right)\right]-\frac{\partial}{\partial x_j}\left(\rho\overline{u_i'u_j'}\right) \tag{2}$$

$$\frac{\partial}{\partial x_j}\left[u_j\left(\rho e+P\right)\right]=\frac{\partial}{\partial x_j}\left[K_{eff}\frac{\partial T}{\partial x_j}+u_i\left(\mu+\mu_t\right)\left(\frac{\partial u_i}{\partial x_j}+\frac{\partial u_j}{\partial x_i}-\frac{2}{3}\delta_{ij}\frac{\partial u_l}{\partial x_l}\right)\right] \tag{3}$$

with i = 1, 2, 3 and j = 1, 2, 3 representing properties in streamwise, vertical, and lateral directions, respectively. Note that x_i (= x_1, x_2, x_3) represent the Cartesian coordinates (x, y, z), respectively, and u_i the time-averaged Cartesian velocity components in the three coordinate directions. The Reynolds stress tensor $\rho\overline{u_i'u_j'}$ in Eq. (2) is given by

$$\rho\overline{u_i'u_j'}=\frac{2}{3}\left(\rho k+\mu_t\frac{\partial u_i}{\partial x_i}\right)\delta_{ij}-\mu_t\left(\frac{\partial u_i}{\partial x_j}+\frac{\partial u_j}{\partial x_i}\right) \tag{4}$$

where μ_t is the turbulent eddy-viscosity, δ_{ij} is the Kronecker delta symbol which is equal to unity when $i = j$ and zero when $i \neq j$, and k is the turbulent kinetic energy $\frac{1}{2}\overline{u_i'u_j'}$. It should be noted here that Eqs. (1)-(3) can be expanded with Einstein's summation rule for repeated indices and two more equations are required to determine μ_t and k for problem closure.

In Eq. (3), the total energy, e, and the effective thermal conductivity, K_{eff}, are given by

$$e=c_p\frac{P}{\rho R}-\frac{P}{\rho}+\frac{\left(u_1^2+u_2^2+u_3^2\right)}{2} \tag{5}$$

$$K_{eff}=K+\frac{c_p\mu_t}{\mathrm{Pr}_t} \tag{6}$$

where K is the thermal conductivity of air and Pr_t is the turbulent Prandtl number taken for air as 0.85. As such, the pressure P is related to the conserved variables through the ideal gas law.

$$P=(\gamma-1)\rho\left[e-\frac{\left(u_1^2+u_2^2+u_3^2\right)}{2}\right]. \tag{7}$$

The molecular viscosity, μ, is calculated from the Sutherland's law given by

$$\frac{\mu}{\mu^*}=\left(\frac{T}{T^*}\right)^{\frac{3}{2}}\frac{T^*+S_0}{T+S_0}. \tag{8}$$

For air, μ^* = 1.716×10^{-5} Pa·s, S_0 = 110.55 K and T^* = 237.11 K .

In the present study, turbulence is modeled by using the realizable k-ε model with enhanced wall treatment. The term "realizable" means that the model satisfies certain mathematical constraints on the Reynolds stresses, consistent with the physics of turbulent flows. The turbulent eddy-viscosity μ_t in this present model is inversely proportional to the dissipation rate ε of turbulent kinetic energy k.

$$\mu_t=\rho C_\mu\frac{k^2}{\varepsilon}. \tag{9}$$

The coefficient C_μ in the above equation is no longer constant as in the case of standard k-ε model. The modeled transport equations for turbulent kinetic energy k and dissipation rate ε are [16]

$$\frac{\partial}{\partial x_j}(\rho k u_j)=\frac{\partial}{\partial x_j}\left[\left(\mu+\frac{\mu_t}{\sigma_k}\right)\frac{\partial k}{\partial x_j}\right]+G_k+G_b-\rho\varepsilon-Y_M \tag{10}$$

$$\frac{\partial}{\partial x_j}(\rho\varepsilon u_j)=\frac{\partial}{\partial x_j}\left[\left(\mu+\frac{\mu_t}{\sigma_\varepsilon}\right)\frac{\partial\varepsilon}{\partial x_j}\right]+\rho C_1 S\varepsilon-\rho C_2\frac{\varepsilon^2}{k+\sqrt{\nu\varepsilon}}+C_{1\varepsilon}\frac{\varepsilon}{k}C_{3\varepsilon}G_b \tag{11}$$

where $C_1=\max[0.43,\frac{\eta}{\eta+5}]$, $\eta=S\frac{k}{\varepsilon}$.

In these equations, G_k represents the generation of turbulence kinetic energy due to the mean velocity gradients. G_b is the generation of turbulence kinetic energy due to buoyancy. Y_M represents the contribution of the fluctuating dilatation in compressible turbulence to the overall dissipation rate. S is average rate coefficient of strain tensor. C_2, $C_{1\varepsilon}$ and $C_{3\varepsilon}$ are constants. σ_k and σ_ε are the turbulent Prandtl numbers for k and ε, respectively.

2.2.2 Energy equation in solid regions

In solid regions, the steady energy transport equation used by ANSYS Fluent has the following form:

$$\frac{\partial}{\partial x_i}\left(K_s\frac{\partial T}{\partial x_i}\right)+S_h=0. \tag{12}$$

In Eq. (12), K_s is the thermal conductivity of the solid material of the bearing disc. S_h is the volumetric heat source, and in this study it is equal to zero.

2.3 Computational grid

In the fluid flow (Fluent) module, using the mesh tool, the structured meshes of the fluid domain and solid domain can be generated, respectively. The final result in the center area of the bearing is shown in Fig. 5. Element size is the most important parameter to control the number and quality of grids, which are shown in Table 4 corresponding to four different element sizes.

It can be seen from Table 4 that the number of grids increases from 1.6 million to 3.85 million while the element size changes from 0.64 mm to 0.40 mm. The average element quality, aspect ratio and Jacobian ratio of the grids change little, but the skewness and warping factor change greatly. The skewness is reduced from 0.0885 to 0.0572, fell by 35.4 per cent. The warping factor is reduced from 1.713×10^{-4} to 1.164×10^{-4}, fell by 32 per cent. Accordingly, it is more appropri-

Table 4. Number and quality of grids based on different element sizes.

	1	2	3	4
Element size (mm)	0.64	0.5	0.45	0.40
Number of grids	1605088	2436301	2984632	3858782
Element quality	0.5303	0.5152	0.5105	0.5140
Skewness	0.0885	0.0708	0.0607	0.0572
Warping factor (×10^{-4})	1.713	1.314	1.229	1.164
Aspect ratio	18.55	17.431	15.767	14.261
Jacobian ratio (MAPDL)	1.167	1.126	1.106	1.093

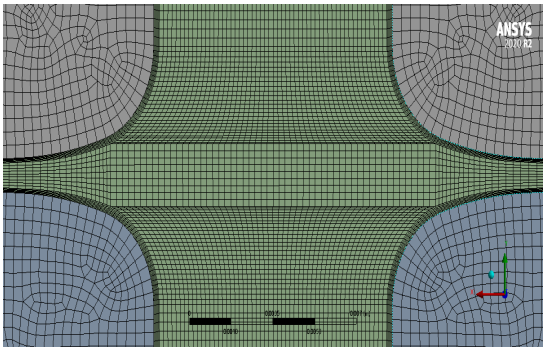

Fig. 5. Grids in the center area of the bearing.

ate to select the fourth group parameter in Table 4. In global mesh control parameters and in local mesh control parameters of solid zone or fluid zone, element sizes are all set as 0.4 mm. The number of elements contained in fluid zone is equal to 1721982, and that contained in solid zone is equal to 2136800. The total number of elements in all of computational domain is 3858782.

The mesh method for overall grid is set as multizone. The size function type is curvature and curvature normal angle is set as 3.0°. The system will automatically determine the size of the mesh element at the refined edge and surface according to the curvature normal angle. The mapped mesh type is set as structured hexa. The maximum layers of inflation are set as 6. The setting method of boundary layer is chosen as smooth transition, and the growth rate is set to 1.2.

2.4 Boundary conditions

2.4.1 Boundary conditions of fluid zone

The boundary surfaces in fluid zone are specified in Fig. 4.

Fluid-solid coupling surfaces (fluid side): It is the interface between fluid zone and solid zone, through which the heat flux of CHT transmits. There are two fluid-solid coupling surfaces denoted as interfacefluidup and interfacefluiddown separately, shown in Fig. 4. These two interfaces are located in the side of fluid.

Pressure-inlet boundary: The pressurized air enters upper anemostat (3) and lower anemostat (10), respectively, so two pressure inlet boundary are defined as upinelt and downinlet, shown in Fig. 4. In the laboratory, the available pressure of the air source system is 50 atm, and the maximum supply pressure of the bearing is 30 atm. In order to obtain the net pressure load on the disc surface, the operating pressure is set to 1 atm. As a result, the total pressure at the inlet flow plane is 29 atm, and ambient back pressure is set to 1 atm. The total temperature at inlet is set as 300.15 K. In the present study, the turbulence intensitiy in the inlet boundary is set to 7 %.

Pressure-outlet boundary: The pressurized air will be issued from exit of the gas film, via the flow channel clearance of aerostatic thrust bearing. The pressure outlet boundary is denoted as outlet, shown in Fig. 4.

Similar to the inlet boundary, the turbulence intensity at the outlet boundary is assumed to be 7 %.

Symmetry plane: As only one half of the whole 3D flow channel is selected, accordingly a symmetrical plane is defined, named symmetryfluid. See Fig. 4.

2.4.2 Boundary conditions of solid zones

The boundary surfaces in solid zones are specified in Fig. 3.

Fluid-solid coupling surfaces (solid side): There are two interfaces located in the side of solid, named interfacesolidup and interfacesoliddown, shown in Fig. 3. The heat from surroundings and internal area of the two discs will pass through the interfaces, and enter the gas film, or vice versa.

Symmetry plane: For upper and lower discs, two symmetrical planes are defined, named symmetrysolidup and symmetrysoliddown, respectively, shown in Fig. 3.

Adiabatic walls: The end surfaces of upper anemostat (3, Fig. 1) and lower anemostat (10, Fig. 1) are defined as adiabatic wall boundary, denoted as wallinletendup and wallinletenddown, respectively. See Fig. 3.

Convective walls: The outside surfaces of anemstats, discs, and the end surfaces of discs opposite to interface of gas film are defined as convective walls, where coefficients of convection heat transfer are set to uniform 10 W/(m^2·K). Those are named walloutsideanemostatup, walloutsideanemostatdown, walloutsidebearingup, walloutsidebearingdown, respectively, shown in Fig. 3.

2.5 Computational method

The calculation process is completed by fluid flow (Fluent) module in ANSYS Workbench 2020R2. In the CHT analysis between gas film and bearing discs, the heat conduction in solid is coupled with convection heat transfer in fluid domain by satisfying the prime boundary condition of continuity of heat flux and temperature field at the solid-fluid interface. Therefore, the most important setting steps are to correctly select the contact region in ANSYS mesh and effectively set up interface of boundary conditions in Fluent.

The numerical scheme selected in the present study is the pressure-velocity coupling SIMPLEC scheme in the general-purpose simulation code designated FLUENT®, which solves the problem more quickly than the SIMPLE scheme.

2.6 Velocity boundary layer and temperature boundary layer in parallel gas film

As for aerostatic thrust bearing with low air supply pressure, it is generally considered that the airflow in the gas film is laminar flow due to fully developed boundary layer and is isothermal flow [17]. However, whether these assumptions are still valid in high-pressure aerostatic thrust bearings requires careful analysis. The clearance airflow in the high-pressure aerostatic thrust bearing is in a very special flow state, since the speed of air in flow channel clearance develops from low subsonic to high subsonic or even supersonic, as already mentioned. The calculated Mach number and static temperature distributions on the symmetric plane of gas film are plotted in Fig. 6.

In Fig. 6, r_h is the radius of the upper or lower air supply hole, r_t is the radius of the throttle of contraction section and r_t = 29.798 mm, as mentioned in Fig. 1. r_e is the radius of discs and r_e = 60 mm. Fig. 6 shows that the velocity of airflow in the flow channel clearance is firstly gradually accelerated from close to 0 to the supersonic at the throttle exit, then decelerated to high subsonic speed, and finally it passes through the outlet of gas film with supersonic speed. According to diverse velocities of the Mach number curve in Fig. 6, there exists an obvious varia-

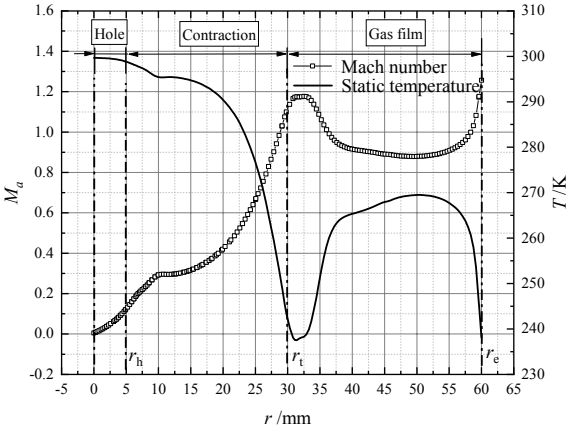

Fig. 6. Flow parameters distribution on the symmetric plane of gas film.

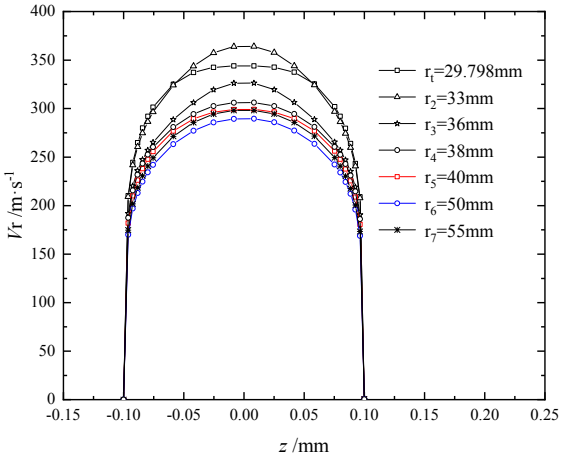

Fig. 7. Pattern of velocity boundary layer in the parallel gas film.

tion of temperature on the symmetric plane of gas film, on which the maximum temperature is 299.66 K and the minimum temperature is 238.08 K. Thus, in the clearance airflow of the high-pressure aerostatic thrust bearing the assumption of isothermal flow is no longer valid.

In order to investigate the pattern of velocity boundary layer development in the parallel gas film, it is necessary to analyze velocity profiles in the gap at different radius vectors, as shown in Fig. 7.

As shown in curve r_t = 29.798 mm in Fig. 7, when the airflow just enters the parallel gas film, due to the rectification effect of the contraction section, the velocity distribution in the center area of the throat of contraction section is relatively uniform, which can be considered as the main stream zone of the flow channel clearance. The velocity profile of the curve r_2 = 33 mm and the curve r_3 = 36 mm are all typical parabolic velocity distribution, which correspond to fully developed laminar flows. Thus, the part region of parallel gas film from r_t to r_2 is the development zone of velocity boundary layer. The part region of parallel gas film from r_2 to r_3 is the fully developed zone of laminar velocity boundary layer, and the velocity on cross section from r_2 to r_3 decreases to a certain extent, corresponding to Fig.

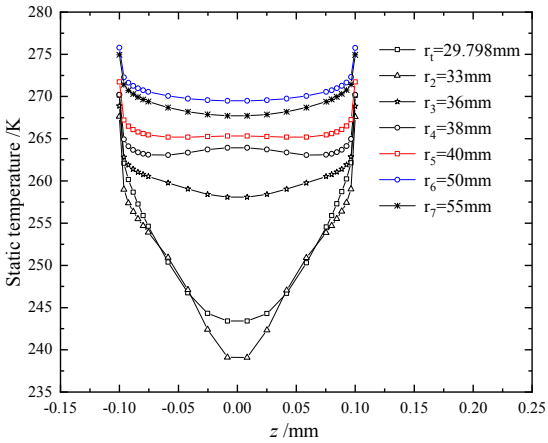

Fig. 8. Pattern of temperature boundary layer in the parallel gas film.

6. The velocity profiles of the curves r_5 = 40 mm, r_6 = 50 mm, r_7 = 55 mm are all subjected to velocity distribution of power law equation, which correspond to a fully developed turbulent flows. Consequently, in the parallel gas film of the high-pressure aerostatic thrust bearing, there are four flow stages with completely different characteristics: boundary layer development zone, fully developed zone of laminar velocity boundary layer, transition from laminar to turbulent and fully developed zone of turbulent boundary layer, which are apparently different from the flow stage in that of aerostatic thrust bearing with low air supply pressure.

The pattern of temperature boundary layer development in the parallel gas film is shown in Fig. 8. As shown in curve r_2 = 33 mm in Fig. 8, the temperature boundary layers on the upper and lower walls do not completely intersect each other, which indicates that the development of the temperature boundary layer is slightly slower than that of the velocity boundary layer. Corresponding to fully developed laminar flows on the cross section at r_3 = 36 mm in Fig. 7, at which the temperature boundary layer is fully developed, as shown in Fig. 8. In the flow transition region of laminar to turbulent (from r_3 = 36 mm to r_5 = 40 mm), the temperature distributions in the central region of the gas film change from concave curves to convex curves, indicating the complex mechanism of the variation of flow regime acting on temperature in that region.

2.7 Temperature field of disc with different materials

For the CHT problem, the heat conduction of the disc and the convective heat transfer interact with each other. Consequently, when we choose different materials to make the bearing disc, the temperature field in the disc and the flow properties in the channel clearance change accordingly. In this study, three common disc materials are considered, whose physical properties are listed in Table 5.

See Table 5, the isotropic thermal conductivity of structural steel is 60.5 W/(m·K), which is the largest among the three

metal materials, while that of invar is the smallest (11 W/(m·K)).

2.7.1 Temperature at interface and symmetric plane of gas film

For the three different materials, the comparison of temperature at the interface between solid disc and airflow in flow channel clearance, and the comparison of temperature at the symmetric plane (14, Fig. 1) of gas film are shown in Fig. 9.

According to change rate of temperature curves in Fig. 9, the high-pressure airflow in the flow channel clearance can be divided into four different regions: a (start of contraction Secs. 7 and 13, Fig. 1), b (adjacent area to the exit of contraction section), c (parallel gas film region), d (adjacent area to the outlet of gas film). Generally, the temperature change rate of region a and c is small, while the temperature in region b and d change sharply, which corresponds to the variation of Mach number in the flow channel clearance.

In Fig. 9, the curve 1, 2, 3 represent the temperature distribution at the interface between solid disc and flow channel, and the curve 4, 5, 6 represent the temperature distribution at symmetric plane of gas film of bearing made of different materials. As is known to all, thermal conductivity indicates the capacity of transmitting heat of certain material. When the temperature gradient of the bearing discs is the same, the material with lager thermal conductivity can transmit more heat than that with smaller thermal conductivity. As is apparent from curve 1, 2, 3 in Fig. 9, the temperature at the interface of structural steel discs is the largest among the three types of materials, which corresponds to its maximum thermal conductivity. As the thermal conductivity of stainless steel and invar is close to each other, the temperature difference at the interface of discs made of these two materials is small. The maximum difference of internal temperature in invar discs is 46.8 K, that in stainless steel discs is 43.2 K and that in structural steel discs is 32.4 K.

From the curve 4, 5, 6 in Fig. 9, we can see that the temperature of region c at the symmetric plane of gas film in structural steel bearing is slightly larger than that in other two cases, which implies that choice of disc material can influence the internal airflow parameters in the channel clearance. However, the effect of different materials' thermal conductivity on the temperature at interface is more remarkable than at the symmetric plane of gas film, as seen in Fig. 9.

Table 5. Physical properties of three common metal materials.

Material name	Stainless steel	Invar	Structural steel
Density (kg/m^3)	7930	8900	7850
Specific heat (J/(kg·K))	500	515	434
Isotropic thermal conductivity (W/(m·K))	16.3	11	60.5
Coefficient of thermal expansion (K^{-1})	1.72×10^{-5}	1.2×10^{-6}	1.2×10^{-5}
Young's modulus (GPa)	193	140	200
Shear modulus (GPa)	74.231	55.118	76.923
Poisson's ratio	0.3	0.27	0.3

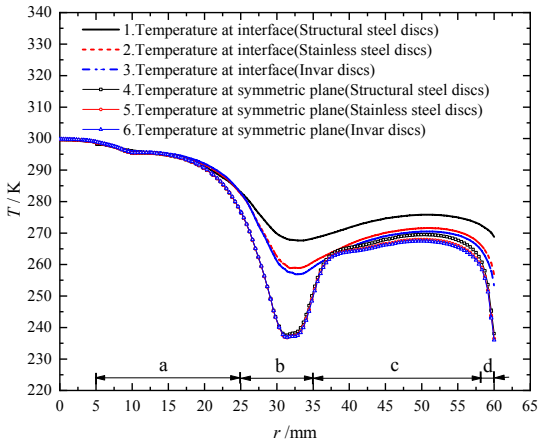

Fig. 9. Temperature at interface and symmetric plane of gas film.

2.7.2 Heat flux via interface

The comparison of heat flux via the interface of different materials is shown in Fig. 10.

Fig. 10 shows the heat flux via the coupling interface of different materials visually. As described in Subsec. 2.7.1, the heat flux via the interface of structural steel discs is apparently larger than that in other two cases, due to its largest thermal conductivity among the three different materials. The overall changing tendency of the curve 1, 2, 3 in Fig. 10 is similar to that in Fig. 9, that is, the heat flux change rate of region a and c is relatively small, while that in region b and d changes sharply.

2.7.3 Temperature distribution in bearing discs

The 3D temperature contour image of upper structural steel disc is shown in Fig. 11.

Fig. 11 vividly shows, on the solid wall adjacent to the gas film, the temperature of the region corresponding to the exit of the contraction section is the lowest, reaching -5.62 °C. In addition, the temperature of the region adjacent to the outlet of the

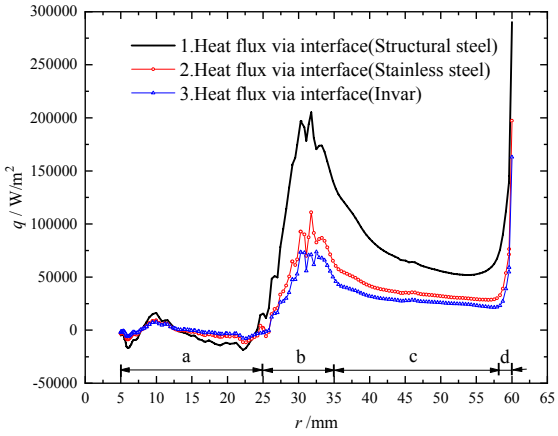

Fig. 10. Heat flux via the interface of different materials.

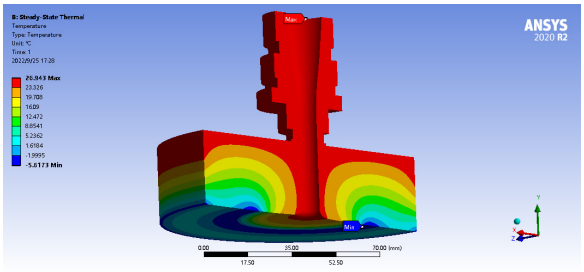

Fig. 11. 3D temperature contour image of upper structural steel disc.

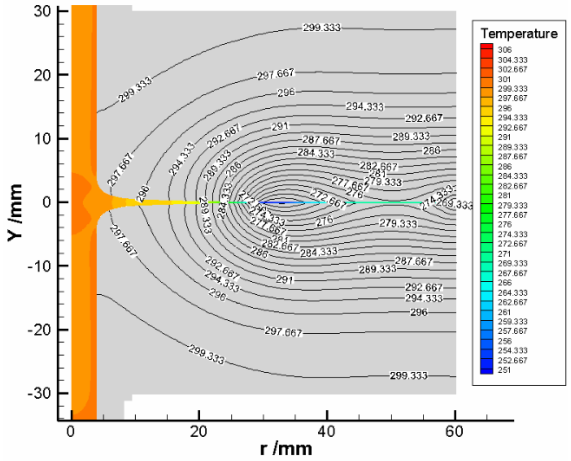

Fig. 12. Temperature contour plots in structural steel discs.

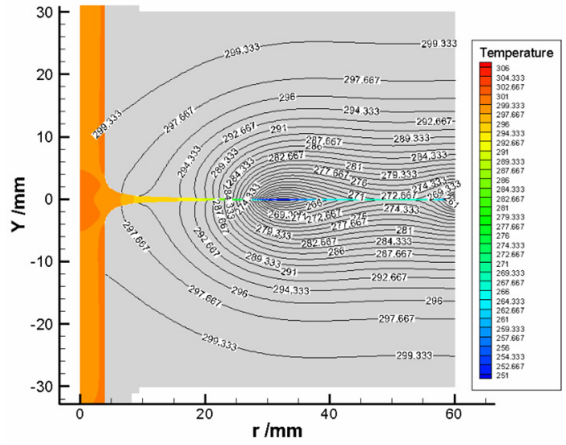

Fig. 13. Temperature contour plots in stainless steel discs.

gas film is also significantly lower than other regions of the disc. In order to further study the temperature gradient of the temperature field of bearing discs, the temperature contour plots in the bearing discs made of three different materials are drawn in Figs. 12-14, respectively. To compare the distribution of isolines in bearing discs with different materials, the same temperature range with [251 K, 306 K] and number of isolines (34 curved lines) are adopted. The temperature difference between any two adjoining isolines is 1.667 K.

As it can be seen from Fig. 9, the minimum temperatures of

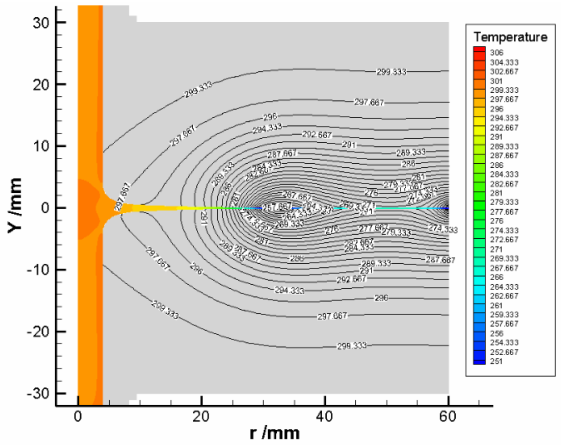

Fig. 14. Temperature contour plots in invar discs.

structural steel disc, stainless steel disc and invar disc are 267.6 K, 256.8 K and 253.2 K, respectively. Therefore, the number of isolines in structural steel discs is minimal, as shown in Fig. 12, while those in invar discs is maximum, as shown in Fig. 14. Correspondingly, the temperature gradient in structural steel discs is relatively gentle, while that in invar discs is obviously sharp, especially in the area adjacent to the exit of contraction section and to the outlet of gas film.

In summary, the thermal conductivity of solid materials is an important factor affecting the temperature gradient inside the bearing discs and the temperature at the interface. At the same time, in CHT, the influencing mechanism of the heat conduction inside the solid on the convection heat transfer in channel clearance lies in the change of heat flux transmitted from solid to airflow and the change of temperature at the interface.

3. Net thermal deformation of bearing disc

3.1 Mathematical model of thermoelasticity

The couple thermoelastic constitutive equations are given by [18]:

$$\{\varepsilon\} = [D]^{-1}\{\sigma\} + \{\alpha\}\Delta T \tag{13}$$

$$S_e = \{\alpha\}^T\{\sigma\} + \frac{\rho_s C_{ps}}{T_0}\Delta T\ . \tag{14}$$

In above two equations, $\{\varepsilon\}$ is total strain vector; S_e is entropy density; $\{\sigma\}$ is stress vector; ΔT is temperature change; T is current temperature; T_0 is absolute reference temperature; $[D]$ is elastic stiffness matrix; $\{\alpha\}$ is vector of total coefficients of thermal expansion; ρ_s is solid density; C_{ps} is solid specific heat at constant pressure.

Using $\{\varepsilon\}$ and ΔT as independent variables, and replacing the entropy density S_e in Eq. (14) with heat density Q which should be expressed in terms of the second law of thermodynamics for a reversible change

$$Q = T_0 S_e \,. \tag{15}$$

We obtain

$$\{\sigma\} = [D]\{\varepsilon\} - \{\beta\}\Delta T \tag{16}$$

$$Q = T_0 \{\beta\}^T \{\varepsilon\} + \rho_s C_{Vs} \Delta T \tag{17}$$

where $\{\beta\}$ is vector of thermoelastic coefficients; C_{Vs} is solid specific heat at constant volume.

Substituting Q from Eq. (17) into the heat flow equation produces

$$\frac{\partial Q}{\partial t} = T_0 \{\beta\}^T \frac{\partial \{\varepsilon\}}{\partial t} + \rho_s C_{Vs} \frac{\partial (\Delta T)}{\partial t} - \left[K^T\right] \nabla^2 T \,. \tag{18}$$

In Eq. (18) $[K^T]$ is thermal conductivity matrix.

Applying the variational principle to stress equation of motion and the heat flow conservation equation coupled by the thermoelastic constitutive equation produces the following finite element matrix equation:

$$\begin{bmatrix} [M] & [0] \\ [0] & [0] \end{bmatrix} \begin{Bmatrix} \{\ddot{u}\} \\ \{\ddot{T}\} \end{Bmatrix} + \begin{bmatrix} [C] & [0] \\ [C^{tu}] & [C^t] \end{bmatrix} \begin{Bmatrix} \{\dot{u}\} \\ \{\dot{T}\} \end{Bmatrix} + \begin{bmatrix} [K^{uu}] & [K^{uT}] \\ [0] & [K^{TT}] \end{bmatrix} \begin{Bmatrix} \{u\} \\ \{T\} \end{Bmatrix} = \begin{Bmatrix} \{F\} + [K^{uT}]\{T_{ref}\} \\ \{Q\} \end{Bmatrix} \tag{19}$$

where $[M]$ is element mass matrix; $[C]$ is element structural damping matrix; $[C^t]$ is element thermal conductivity matrix; $[C^{tu}]$ is element thermoelastic damping matrix; $[K^{uu}]$ is element stiffness matrix; $[K^{uT}]$ is element thermoelastic stiffness matrix; $[K^{TT}]$ is element thermal conductivity matrix; $\{u\}$ is displacement vector; $\{F\}$ is sum of the element nodal force and element pressure vectors; $\{T\}$ is temperature vector; $\{Q\}$ is sum of the element heat generation load and element convection surface heat flow vectors.

It is noted that when we temporarily ignore the pressure load exerted by the gas film on the surface of the bearing discs, the research object is simplified to a net thermoelastic deformation problem. Correspondingly, the element pressure vector in $\{F\}$ is a zero vector.

3.2 Computational workflow

For net thermoelastic analysis in this study, three analysis modules are required. They are fluid flow (Fluent), steady-state thermal, and static structural, respectively. Although the internal temperature distribution in bearing discs has been solved in analysis of CHT by fluid flow (Fluent) module, the result data format of the finite volume method in that cannot be directly matched to format request of input data of static structural module. Therefore, it is needed to solve it again in steady-state thermal module, and then input the calculation result data of that into static structural module. The workflow of data transmission among three modules is shown in Fig. 15.

First, calculate the CHT in fluid flow module. Then set the boundary conditions of the steady-state thermal module and resolve 3D temperature field of the bearing discs. Finally set the boundary conditions of static structural module and complete the calculation of net thermoelastic deformation of the discs.

3.3 Computational grid

As shown in Fig. 15, the grid generation tool of the fluid flow module is independent, named as 'mesh', while the grid generation tool of steady-state thermal module is integrated in the modeling tool. The overall grid of bearing discs is shown in Fig. 16.

The default physics preference is set to be 'mechanical', element size is set to be 1.0 mm, and resolution is set to be 5. In transition drop-down list, set the option to 'fast', and set the option to 'fine' in span angle center drop-down list. The number of elements in two discs is equal to 234154. In order to reduce the interpolation error of result data of temperature load, the same meshing parameters are maintained in steady-state thermal module and static structural module.

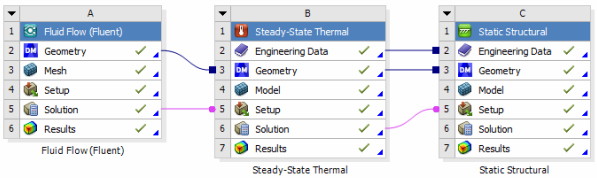

Fig. 15. Workflow for net thermoelastic analysis.

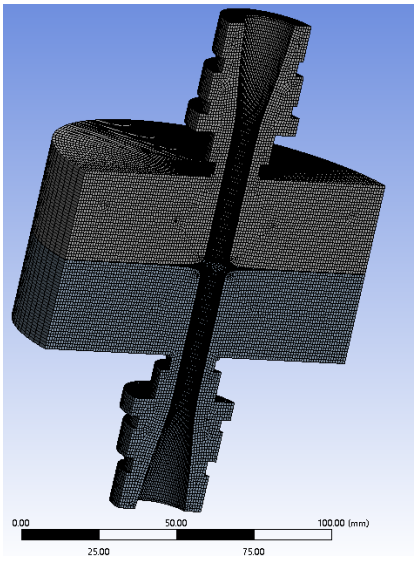

Fig. 16. Overall grid of bearing discs in steady-state thermal module.

3.4 Boundary conditions

3.4.1 Boundary conditions in steady-state thermal module

As the temperature results of all external surfaces of bearing discs have been solved in calculation of CHT analysis by fluid flow (Fluent) module, which should be used for temperature boundary conditions in steady-state thermal module, listed in Table 6. These boundary conditions of wall temperature can be exerted onto the solid model in the form of temperature load on the specified surfaces, and the corresponding temperature data can be directly imported from results data of fluid flow (Fluent) module to steady-state thermal module. As a result, a heat conduction problem with specified wall temperature is solved in steady-state thermal module.

3.4.2 Boundary conditions in static structural module

There are two types of calculation conditions for net thermoelastic analysis. One is the internal 3D temperature distribution of the bearing discs, and the other is the constraint condition of the bearing discs. The former can be directly imported from the results data of the steady-state thermal module to static structural module, and the latter is set to fixed support on the second cylindrical surface.

3.5 Net thermoelastic deformation of disc with different materials

In order to compare thermoelastic deformation of three discs with different materials, a path in upper disc is defined along the profile of contraction section and parallel gas film, as shown in Fig. 17.

The deformation curves in Y direction on the path of upper bearing disc made of different materials are shown in Fig. 18.

It can be seen from Table 5 that density and specific heat of three materials are close to each other. As a consequence, in mathematical model of thermoelastic problem such as Eqs. (13)-(19), the main factors affecting thermoelastic deformation are only the coefficient of thermal expansion and temperature change. Apparently, in Table 5 the coefficient of thermal expansion of invar disc is one order of magnitude smaller than that of stainless steel disc, while the variation of maximum difference of internal temperature in three types of discs is not significant. The maximum difference of internal temperature in invar disc is 14.4 K greater than that in structural steel disc. Finally, the coefficient of thermal expansion is the dominant factor determining the size of net thermoelastic deformation of the bearing disc.

In Fig. 18, the net thermoelastic deformation of stainless steel disc is the largest (25.7 μm), corresponding to its greatest coefficient of thermal expansion (1.72×10^{-5} K^{-1}). The net thermoelastic deformation of invar disc is the smallest (1.86 μm), corresponding to its smallest coefficient of thermal expansion (1.2×10^{-6} K^{-1}). This is also the reason why invar is called low expansion alloy. From Figs. 11-14 it shows that the low temperature region of bearing disc is mainly concentrated in the area adjacent to parallel gas film, which shrinks significantly, leading to the overall downward bending deformation of the path, as shown in Fig. 18.

The 3D deformation contours of upper stainless steel disc is shown in Fig. 19.

Surprisingly, the minimum deformation point in upper disc is

Table 6. Boundary conditions of heat conduction.

External surface of upper anemostat	Specified wall temperature
External surface of lower anemostat	Specified wall temperature
Inlet end face of upper anemostat	Specified wall temperature
Inlet end face of lower anemostat	Specified wall temperature
External surface of upper disc	Specified wall temperature
External surface of lower disc	Specified wall temperature
Interface between fluid and upper disc parts, at solid side	Specified wall temperature
Interface between fluid and lower disc parts, at solid side	Specified wall temperature

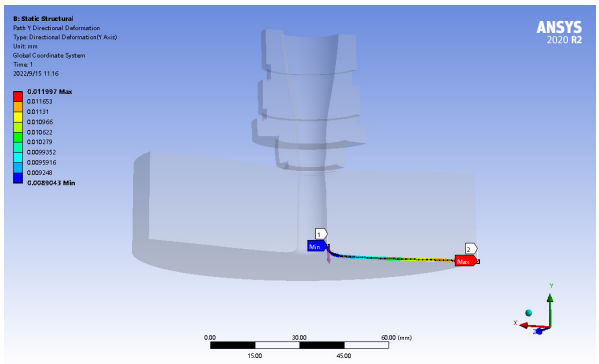

Fig. 17. The path defined for postprocessing.

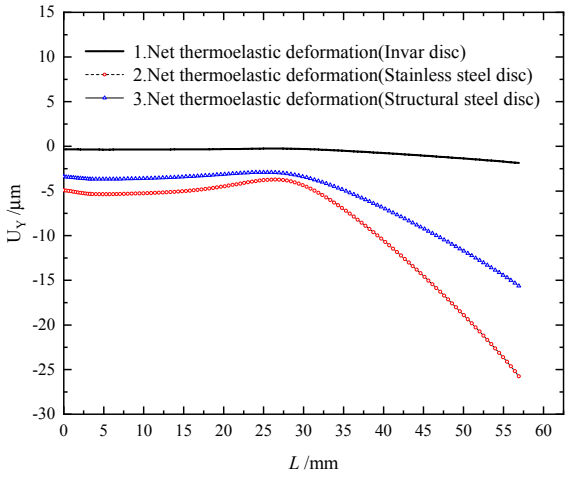

Fig. 18. The net thermoelastic deformation in Y direction on the path.

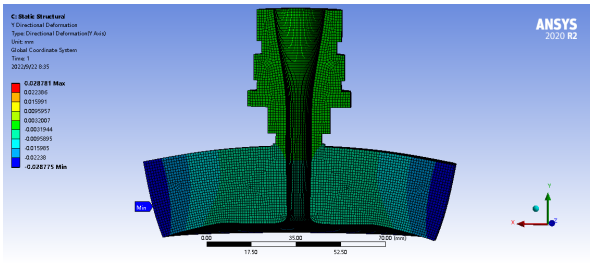

Fig. 19. The 3D thermoelastic deformation in Y direction of upper stainless steel disc.

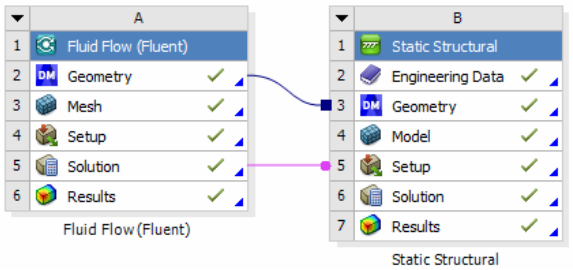

Fig. 20. Workflow for calculating net elastic deformation.

not on its lower end face, but on the point slightly lower the middle point of outer cylindrical surface, as shown in Fig. 19.

4. Net elastic deformation of bearing discs caused only by gas film pressure

The structural elastic deformation caused by gas film pressure is a common engineering problem, and its mathematical model can be consulted from many relevant references.

4.1 Computational workflow

For net elastic deformation of bearing disc caused only by gas film pressure in this study, two analysis modules are required. they are fluid flow (Fluent) and static structural, respectively, as shown in Fig. 20.

As shown in Fig. 20, the Workbench platform makes the transmission of result data of pressure load on the structural surface very convenient, and the constraint condition of the bearing discs in static structural module is the same as that in Subsec. 3.4.2.

4.2 Net elastic deformation of discs with different materials

The net structural elastic deformation curves caused only by gas film pressure in Y direction on the path of upper bearing disc made of different materials are shown in Fig. 21.

It can be seen from Table 5 that Young's modulus and shear modulus of invar disc are both the smallest among the three types of materials, so its net elastic deformation caused only by gas film pressure is the largest, as shown in Fig. 21. Young's modulus and shear modulus of stainless steel and structural steel discs are close to each other. As a result, their net elastic deformations are close to each other too, as shown in Fig. 21.

It is worth noting that the sign of net elastic deformation of upper disc caused only by gas film pressure is positive in Fig. 21, while the sign of net thermoelastic deformation of upper disc caused by the uneven temperature field is negative in Fig. 18. Therefore, the deformation direction caused by above two factors is opposite, which can offset part of the deformation. Apparently, the comparison of Figs. 18 and 21 suggests that the elastic deformation by pressure is the dominant factor in

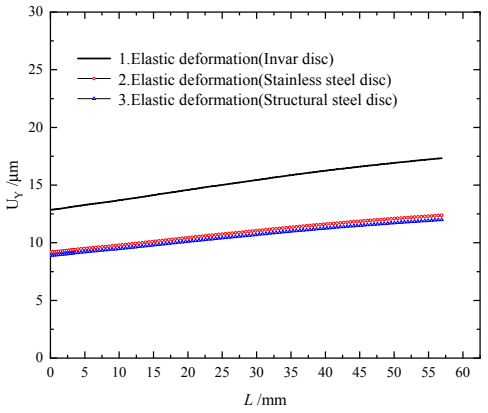

Fig. 21. The net elastic deformations in Y direction on the path.

the total deformation of invar disc, while the thermoelastic deformation is the minor factor. For stainless steel and structural steel discs, the reverse is true.

5. Total deformation of bearing disc

5.1 Mathematical model

When we study the total deformation of the bearing disc, the mathematical model of this problem is similar to the net thermoelastic deformation problem in Subsec. 3.1. The difference is only that the element pressure vector in $\{F\}$ in Eq. (19) is non-zero vector.

5.2 Computational workflow

For the analysis of total deformation of bearing disc, three analysis modules are required, which is similar to Fig. 15. The workflow of data transmission among three modules is shown in Fig. 22.

As shown in Fig. 22, the difference between workflow for total deformation analysis and that for net thermoelastic deformation analysis only lies in whether the pressure load data of the gas film is applied to the static structural module.

5.3 Total deformation of disc with different materials

The total deformation curves caused by pressure of gas film

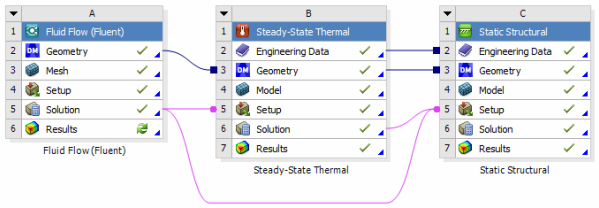

Fig. 22. Workflow for total deformation of the bearing disc.

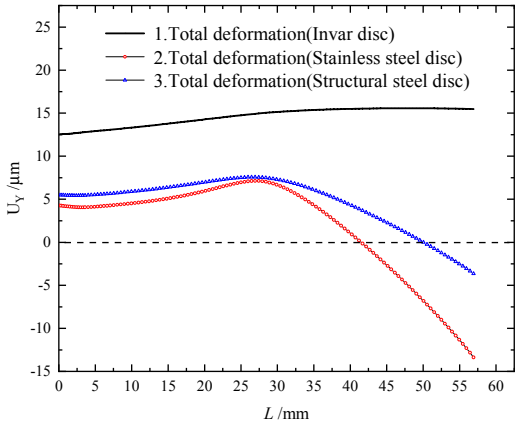

Fig. 23. The total deformations in Y direction on the path.

and uneven temperature field in Y direction on the path of upper bearing disc made of different materials are shown in Fig. 23.

According to Fig. 23, the sign of total deformation of upper invar disc is always positive, which mainly originates from its elastic deformation caused by gas film pressure. Its net thermoelastic deformation is almost negligible, and its maximum absolute amount of total deformation is 15.47 μm. For upper stainless steel and structural steel disc, the sign of the total deformation of the central region of the disc is positive, which similarly stems from their elastic deformation caused by pressure, while the direction of total deformation of the area corresponding to parallel gas film is reverse. Their maximum absolute amount of total deformation is 13.37 μm and 7.56 μm, respectively. Consequently, the maximum absolute amount of total deformation of upper structural steel bearing disc accounts for only half of that of invar disc or stainless steel disc.

As is known to all, among the three materials, the unit price of structural steel is the cheapest, and that of invar is the most expensive. As for the working conditions of pressure and temperature load specified in this study, structural steel is a reasonable choice for material of bearing disc, at the same time, it is also the most economical one. This once again verifies the principle of material selection in the design of mechanical parts, that is, materials should be selected according to the using performance of actual parts, instead of the random advantages of a certain physical property of materials.

6. Conclusions

In this study, based on the coupling analysis of the air flow field in the channel clearance of the high-pressure aerostatic thrust bearing and the CHT of the bearing discs, the development process and flow regime of the velocity boundary layer and the temperature boundary layer in the parallel gas film are investigated. Subsequently, a comprehensive coupling thermal deformation investigations of the bearing is simplified to the combination of a steady CHT problem and a static thermoelastic deformation problem. The effects of the thermal conductivity of the solid material on the temperature gradient inside the bearing discs, and on the temperature distribution at the coupling interface or in the gas film of channel clearance are emphatically investigated. The influencing mechanism between the relevant material physical properties and thermal deformation of the bearing discs in uneven temperature field is analyzed in detail. The major conclusions are drawn as follows:

1) In the parallel gas film of the high-pressure aerostatic thrust bearing, there are four flow stages with completely different characteristics: boundary layer development zone, fully developed zone of laminar velocity boundary layer, transition from laminar to turbulent and fully developed zone of turbulent boundary layer, which are apparently different from the flow stage in that of aerostatic thrust bearing with low air supply pressure.
2) In CHT of this type of bearing, the thermal conductivity of solid material is an important factor affecting the temperature gradient inside the bearing disc and the temperature at the interface, variation of which can change heat flux via interface and the temperature at interface significantly.
3) The coefficient of thermal expansion of the material is a crucial parameter that affects the net thermoelastic deformation of the bearing discs, but its final total deformation also depends on the pressure load it receives. Therefore, it cannot be taken for granted that the smaller the coefficient of thermal expansion is, the smaller the total deformation of the disc will be.
4) As for the working conditions of pressure and temperature load specified in this study, structural steel is a reasonable choice for material of bearing disc, and it is also the most economical choice.

Acknowledgments

This work is supported by the National Natural Science Foundation of China (Grant No. 51475341).

Nomenclature

k : Turbulent kinetic energy
K : Kelvin temperature scale
K : Thermal conductivity of air
K_s : Thermal conductivity of the solid material
K_{eff} : Effective thermal conductivity
μ : Molecular viscosity
μ^* : Viscosity coefficient at reference temperature
μ_t : Turbulent eddy-viscosity

T : Temperature
T^* : Reference temperature in sutherland equation
T_0 : Absolute reference temperature
S : Average rate coefficient of strain tensor
S_0 : Sutherland constant
S_h : Volumetric heat source
S_e : Entropy density

References

[1] K. Sim, Y. B. Lee, J. W. Song and T. H. Kim, Effect of cooling flow on thermal performance of a gas foil bearing floating on a hot rotor, *Journal of Mechanical Science and Technology*, 32 (5) (2018) 1939-1954.

[2] S. Ohishi and Y. Matsuzaki, Experimental investigation of air spindle unit thermal characteristics, *Precision Engineering*, 26 (2002) 49-57.

[3] D. J. Han, C. L. Tang, L. Hao and J. F. Yang, Experimental studies on the effects of bearing supply gas pressure on the response of a permanent magnet disk-type motor rotor, *Journal of Mechanical Science and Technology*, 30 (11) (2016) 4887-4892.

[4] Q. Gao, L. H. Lu, R. Zhang, L. Y. Song, D. H. Huo and G. L. Wang, Investigation on the thermal behavior of an aerostatic spindle system considering multi-physics coupling effect, *International J. of Advanced Manufacturing Technology*, 102 (2019) 3813-3823.

[5] K. Sim, Y. B. Lee, S. M. Jang and T. H. Kim, Thermal analysis of high-speed permanent magnet motor with cooling flows supported on gas foil bearings: part II-bearing modeling and case studies, *Journal of Mechanical Science and Technology*, 29 (12) (2015) 5477-5483.

[6] F. Xu and L. B. Guo, Design theory of the contraction cone of circular thrust gas bearings in high supply pressure, *Machinery Design and Manufacture*, 54 (7) (2017) 30-32 (in Chinese).

[7] J. S. Li and P. K. Liu, Dynamic analysis of 5-DOFs aerostatic spindles considering tilting motion with varying stiffness and damping of thrust bearings, *Journal of Mechanical Science and Technology*, 33 (11) (2019) 5199-5207.

[8] Q. Li, S. Zhang, L. Ma, W. W. Xu and S. Y. Zheng, Stiffness and damping coefficients for journal bearing using the 3D transient flow calculation, *Journal of Mechanical Science and Technology*, 31 (5) (2017) 2083-2091.

[9] A. Afzal, A. Samee and R. Razak, Steady and transient state analyses on conjugate laminar forced convection heat transfer, *Archives of Computational Methods in Engineering*, 27 (2020) 135-170.

[10] D. Konar, M. Sultan and S. Roy, Numerical analysis of 2-D laminar natural convection heat transfer from solid horizontal cylinders with longitudinal fins, *International Journal of Thermal Sciences*, 154 (2020) 1-13.

[11] X. Wang, H. Z. Xu and J. H. Wang, Multi-objective optimization of discrete film hole arrangement on a high pressure turbine end-wall with conjugate heat transfer simulations, *International Journal of Heat and Fluid Flow*, 78 (2019) 1-13.

[12] A. S. Dorfman, *Applications of Mathematical Heat Transfer and Fluid Models in Engineering and Medicine*, John Wiley & Sons Publishing Company, New York, USA (2017).

[13] M. C. Murty, P. Manna and D. Chakraborty, Conjugate heat transfer analysis in high speed flows, *Proc. Inst. Mech. Eng. G J. Aerosp. Eng.,* 227 (10) (2013) 1672-1681.

[14] K. Marimuthu, K. Umanath and S. J. Krishnan, Investigating the conjugate heat transfer phenomena on various ducts for aircraft environmental control system, *Materials Today: Proceedings,* 46 (2021) 3631-3638.

[15] M. E. Eleshaky, CFD investigation of pressure depressions in aerostatic circular thrust bearings, *Tribology International*, 42 (2009) 1108-1117.

[16] Ansys Inc., *Ansys Fluent Theory Guide, Ansys 2020R2*, Ansys Inc., USA (2020).

[17] W. A. Gross, L. A. Matsch and V. Castelli, *Fluid Film Lubrication*, John Wiley & Sons Publishing Company, New York, USA (1980).

[18] Ansys Inc., *Ansys Mechanical APDL Theory Reference, Ansys 2020R2*, Ansys Inc., USA (2020).

Liangbin Guo received M.Eng. from Wuhan University of Science and Technology, Wuhan, China in 2000 and Ph.D. degrees from Harbin Institute of Technology, Harbin, China in 2005. He is currently a Professor with School of Machinery and Automation, Wuhan University of Science and Technology, Wuhan, China. His current research interests include design of high-pressure aerostatic and fluid-thermo-structural coupling investigations of it.